Alkaline Water Splitting Enhancement by MOF-Derived Fe–Co–Oxide/Co@NC-mNS Heterostructure: Boosting OER and HER through Defect Engineering and In Situ Oxidation

Thangjam Ibomcha Singh, Gaddam Rajeshkhanna, Uday Narayan Pan, Tolendra Kshetri, Han Lin, Nam Hoon Kim,* and Joong Hee Lee*

Introducing defects and in situ topotactic transformation of the electrocatalysts generating heterostructures of mixed-metal oxides(hydroxides) that are highly active for oxygen evolution reaction (OER) in tandem with metals of low hydrogen adsorption barrier for efficient hydrogen evolution reaction (HER) is urgently demanded for boosting the sluggish OER and HER kinetics in alkaline media. Ascertaining that, metal–organic-framework-derived freestanding, defect-rich, and in situ oxidized Fe–Co–O/Co metal@N-doped carbon (Co@NC) mesoporous nanosheet (mNS) heterostructure on Ni foam (Fe–Co–O/Co@NC-mNS/NF) is developed from the in situ oxidation of micropillar-like heterostructured Fe–Co–O/Co@NC/NF precatalyst. The in situ oxidized Fe–Co–O/Co@NC-mNS/NF exhibits excellent bifunctional properties by demanding only low overpotentials of 257 and 112 mV, respectively, for OER and HER at the current density of 10 mA cm^{-2}, with long-term durability, attributed to the existence of oxygen vacancies, higher specific surface area, increased electrochemical active surface area, and in situ generated new metal (oxyhydr) oxide phases. Further, Fe–Co–O/Co@NC-mNS/NF (+/−) electrolyzer requires only a low cell potential of 1.58 V to derive a current density of 10 mA cm^{-2}. Thus, the present work opens a new window for boosting the overall alkaline water splitting.

T. I. Singh, Dr. U. N. Pan, Dr. T. Kshetri, Prof. N. H. Kim, Prof. J. H. Lee
Department of Nano Convergence Engineering
Jeonbuk National University
567, Baekje-daero, Deokjin-gu, Jeonju-si, Jeollabuk-do 54896, Republic of Korea
E-mail: nhk@jbnu.ac.kr; jhl@jbnu.ac.kr

T. I. Singh, Dr. H. Lin
Centre for Translational Atomaterials
Faculty of Science, Engineering and Technology
Swinburne University of Technology
PO Box 218, Hawthorn, VIC 3122, Australia

Dr. G. Rajeshkhanna
Department of Chemistry
National Institute of Technology Warangal
Warangal, Telangana 506004, India

Prof. J. H. Lee
Carbon Composite Research Centre
Department of Polymer – Nano Science and Technology
Jeonbuk National University
Jeonju, Jeonbuk 54896, Republic of Korea

1. Introduction

Hydrogen production through electrochemical means, such as conventional electrolysis or solar photoelectrochemical water splitting, coupled to various other renewable energy sources (e.g., solar or wind) is considered to be the future of energy.[1] However, the oxygen evolution reaction (OER) at the anode has sluggish kinetics of four-electron-coupled reactions and demands high overpotentials to overcome the uphill kinetic barriers.[2] Besides, the hydrogen evolution reaction (HER) at the cathode is also relatively sluggish in alkaline media compared to that in acidic media and similarly demands highly active electrocatalysts.[3] Thus, the development of effective bifunctional electrocatalysts, highly active for both OER and HER, is currently pursued in various ways to increase their electrocatalytic activities. So far, IrO$_2$ and RuO$_2$ are considered as the state-of-the-art OER electrocatalysts, whereas platinum (Pt) is the best HER electrocatalyst.[4] However, their large-scale use for sustainable H$_2$ production is not possible, because of their high cost and scarcity. Accordingly, various nonprecious-metal-based electrocatalysts were investigated for improving the OER and HER activities. The first-row transition-metal oxides, especially the cobalt-based oxides, such as Co$_3$O$_4$ and CoO, with high OER activity, have attracted great attention over the years as cheap, abundant, and durable electrocatalysts.[5] Also, metallic cobalt (Co) has low energy barriers for hydrogen adsorption, indicating its potential for HER activities.[6] Therefore, heterostructures of cobalt-based oxides and metallic Co can exhibit promising bifunctional electrocatalytic properties for overall water splitting. However, the pristine cobalt oxides such as Co$_3$O$_4$ showed low conductivity and easy aggregation that reduce the active sites and retard the charge transport during the electrochemical process. To tackle the limitation, highly porous and conducting carbon materials, such as graphene, reduced graphene oxide (rGO), and carbon nanotubes, with large specific surface area (SSA) have been employed to support such materials for the advancement of Co-based electrocatalysts by developing metal/metal oxide@carbon heterostructures.[7,8] But, complex and multistepped procedures, nonuniform distribution of the

**ADVANCED
SCIENCE NEWS**
www.advancedsciencenews.com

NANO · MICRO
small
www.small-journal.com

active metal/metal oxides on the carbon supports, and much agglomeration in such composite electrocatalysts still hindered its overall water-splitting efficiency. So, the development of new sustainable metal/metal oxide@carbon hybrid heterostructures with high OER and HER bifunctional electrocatalytic activities through simple and inexpensive processes is urgently needed for large-scale hydrogen production.

Metal–organic frameworks (MOFs), in this regard, serve as important precursor materials to derive a variety of advanced materials with 3D superstructures and 2D nanosheets, exhibiting high SSA with tunable compositions.[9,10] During the carbonization of MOFs in an inert gas atmosphere, the metallic components can give rise to metal/metal oxides, while the organic components are converted to various forms of carbon, yielding various types of metal/metal oxides@carbon hybrid heterostructures with high SSA and high porosity.[10,11] Such electrocatalysts with 3D superstructures and 2D nanosheets exhibit large active sites and improve mass-transfer rates because of their high SSA and high porosity.

Furthermore, the electrocatalytic activity can be additionally increased by tuning the electronic structure via doping, alloying, defect engineering, oxygen-vacancy creations, etc.[12] The OER performance is heavily influenced by water-adsorption capability and the electrical conductivity of the catalysts, which are strongly correlated to their electronic configurations, especially the electron delocalization.[12–14] In this regard, defect engineering has been adopted as a potential approach to cause electron delocalization.[13] Currently, as one of the most studied types of defect engineering, oxygen vacancy creations in transition metal oxides can facilitate electrochemical water splitting by activating the neighboring atoms, causing the antibonding orbitals to shift upward toward the Fermi level, thereby providing extra electronic states around the Fermi level and increasing the reactivity of the catalytically active sites.[12,15,16] This eventually increases the oxygen adsorption and accelerates the charge-transfer process, enabling superior OER/HER activities.[12] Recent operando studies of Co_3O_4 having rich oxygen vacancies also showed that oxygen vacancies were initially filled with OH* and can increase the preoxidation of low-valent cobalt species even at low applied potentials, resulting in electrocatalysts' surface reconstruction prior to OER.[15] Further, the catalytic activities can also be improved by tuning of the metal-coordination environment electrochemically in hydrolytic and harsh alkaline media.[17] Electrocatalysts undergo superficial oxidation to their oxides or oxyhydroxides under the alkaline conditions during their electrochemical tests, especially OER.[18] A recent study showed that cobalt oxide Co_3O_4 nanoparticles undergo an in situ transformation of cobalt (oxyhydr)oxide-like phase during OER.[18] Interestingly, such in situ oxidized electrocatalysts exhibited better electrocatalytic activities with low overpotential, exhibiting fast OER kinetics than pristine hydroxides or oxides.[15,17,18] Another effective method to increase the electrocatalytic activities is incorporating secondary elements such as Fe in the host Co-based materials. Incorporation of Fe facilitates easy OH^- intercalation into layered (oxy)hydroxide, creates defect-generating active sites, and improves the electrical conductivity of the Co-host material, boosting OER.[19] So, it is highly anticipated that a tandem structure of Co- and Fe-based metal/metal oxide@N-doped carbon heterostructures

exhibiting both 3D and 2D natures with oxygen vacancies may also be in situ oxidized to generate new catalytically active species for efficient overall water splitting. However, due to the complexity of developing such electrocatalysts, there has not been such a report, best to our knowledge.

So, inspired by the motivation gathered from the literature, in this work, we have for the first time developed Fe–Co–oxide/Co-metal@N-doped carbon hybrid heterostructured electrocatalysts on Ni foam (Fe–Co–O/Co@NC/NF) following a thermal decomposition of FeCo–Prussian blue analog (PBA) under Ar atmosphere at 800 °C. The developed Fe–Co–O/Co@NC/NF showed oxygen vacancies caused by high-temperature annealing in an inert atmosphere and acted as a precatalyst undergoing in situ oxidation during the OER evaluations. The in situ oxidation resulted in morphological changes from micropillar-like structures to thin nanosheets and introduced structural defects, with superficially oxidized oxyhydroxides as new active species. The in situ oxidized Fe–Co–O/Co@NC mesoporous nanosheet (mNS) on the Ni foam (Fe–Co–O/Co@NC-mNS/NF) acts as a new class of bifunctional electrocatalysts, exhibiting a very low overpotential for OER, HER, and overall water-splitting applications.

2. Results and Discussions

2.1. Physical Characterization of the Electrocatalysts

The development of the electrocatalysts is shown by the schematic in **Figure 1**. We developed the Fe–Co–O/Co@NC/NF electrocatalyst using Co–MOF grown on Ni foam (Co–MOF/NF) as the starting material, followed by an anion exchange reaction with $K_3(Fe(CN)_6)$ aqueous solution forming FeCo–PBA and its subsequent annealing under Ar atmosphere. After an anion exchange reaction in the aqueous $K_3(Fe(CN)_6)$ solution, field-emission scanning electron microscopy (FE-SEM) analysis revealed that the micropillar-like morphology of Co–MOF/NF was transformed into a highly defect-rich surface nanostructured FeCo–PBA/NF (Figures S1 and S2, Supporting Information), as in our previous report.[9] When FeCo–PBA/NF was annealed in Ar at 800 °C, the overall vertical micropillar-like morphology was still preserved with slight surface deformations caused by the decomposition of the organic component in the framework (**Figure 2**A_1–A_3). The nanospikes on the surface of FeCo–PBA micropillars were converted into nanogranule-like structures (FE-SEM image, Figure 2A_2,A_3). However, after subjecting it to various cyclic voltammetry (CV) cycles and the long-term chronopotentiometry after the evaluation of OER activities, we found that the Fe–Co–O/Co@NC/NF underwent drastic surface reconstruction, giving rise to a new mNS structure (Figure 2B_1–B_3). As can be seen from the FE-SEM images (Figure 2B_1–B_3), the in situ oxidized Fe–Co–O/Co@NC-mNS/NF showed highly uniform and extremely porous nanosheet structures (Figure 2B_2,B_3) compared to that of Fe–Co–O/Co@NC/NF (Figure 2A_2,A_3). Such morphological transformation can be attributed to the oxidation of Co species and their topotactic transformation,[20] and the associated in situ generated tensile stress and strain during the potential cycling.[2,21]
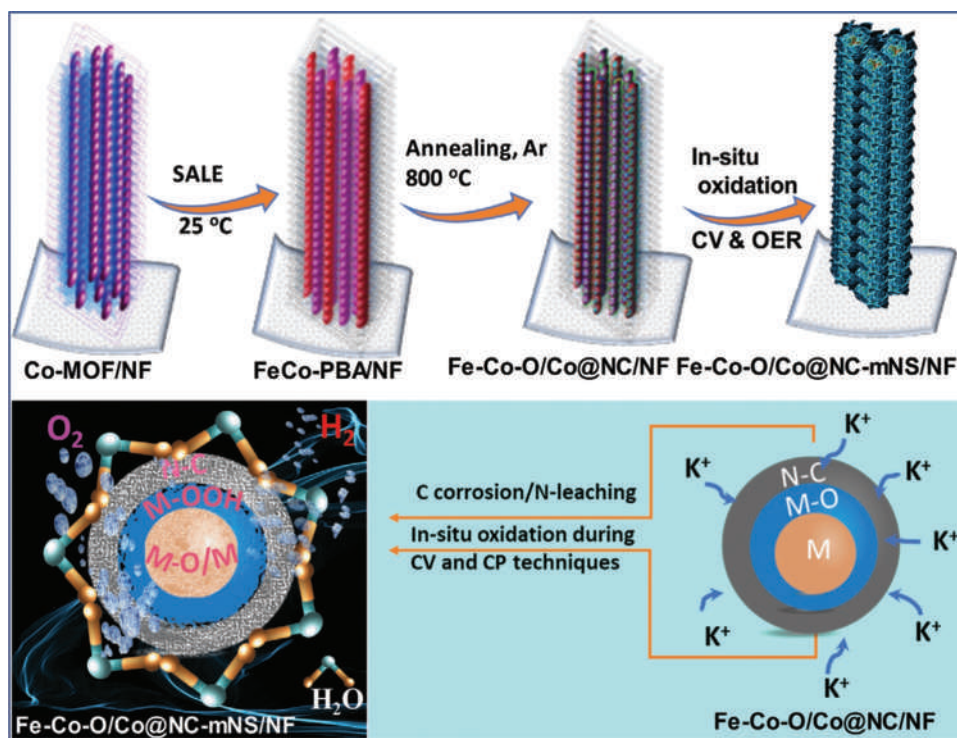
Figure 1. Schematic diagram representing the development of the Fe–Co–O/Co@NC/NF hybrid electrode from Co–MOF/NF as starting material and the in situ electrochemical transformation to the in situ oxidized mesoporous nanosheet (mNS) structures (denoted as Fe–Co–O/Co@NC-mNS/NF) with the plausible mechanism for the in situ oxidation.

The presence of highly porous empty nanospaces between the interconnecting nanosheets (Figure 2B₃) is highly beneficial for diffusion of the electrolytes and interaction with the active sites on the surface of the electrocatalysts. We expected this transformation of the morphology from micropillar-like structures to interconnected large mesoporous nanosheets to highly increase the exposed active sites available for electrocatalytic activities. Further, energy dispersive X-ray (EDX) spectra and the corresponding elemental atomic concentration percentage showed lower oxygen (14.20 at%) for Fe–Co–O/Co@NC/NF (Figure 2C₁) than for the in situ oxidized Fe–Co–O/Co@NC-mNS/NF electrocatalysts (42.28 at%) (Figure 2C₂), implying the occurrence of in situ electrochemical oxidation. The presence of additional peaks around 2.0 keV (Figure 2C₁,C₂) correspond to sputtered Pt on the samples to improve their conductivity for better FE-SEM measurement and the peak at 3.5 keV (Figure 2C₂) is due to potassium (K) impurities left on the electrocatalyst's surface after the electrochemical evaluations in KOH electrolyte. The lower oxygen content of Fe–Co–O/Co@NC/NF could arise because of the removal of lattice oxygen caused by the bombardment at high-temperature annealing in inert Ar atmosphere, enabling oxygen vacancy formation.[22]

Besides the morphological transformation observed, we also assessed the changes in the phase of the electrocatalysts from the corresponding powder X-ray diffraction (P-XRD) patterns. The P-XRD patterns of Fe–Co–O/Co@NC/NF showed main peaks at 2θ values of 18.25°, 29.97°, 35.41°, 36.45°, 42.36°, 43.98°, 51.23°, 53.20°, 56.89°, 61.43°, 62. 51°, 73.61°, 75.53°, and

77.49° (**Figure 3**A). The dominant peaks at 2θ values of 43.98°, 51.23°, and 75.53° were matched with that of the (111), (020), and (022) planes, respectively, of cubic Co_4 (JCPDS-ICCD: 96-901-1619) (Figure 3A), whereas the peaks at 18.25°, 29.97°, 35.41°, 43.01°, 56.89°, 62.51°, 73.81° could be indexed to the (111), (022), (131), (040), (151), (044), and (353) planes, respectively, of cubic $Fe_{2.38}Co_{0.62}O_4$ (JCPDS-ICCD: 96-153-4942) (Figure 3A). The peaks at 36.45°, 42.36°, 61.43°, 73.61°, 77.49° could be assigned to the (111), (200), (220), (311), and (222) planes, respectively, of cubic CoO (JCPDS-ICCD: 01-078-0431) (Figure 3A). This shows that Fe–Co–O/Co@NC/NF was composed of metallic Co_4, CoO, and mixed Fe–Co–O phases (Figure 3A). For the in situ oxidized Fe–Co–O/Co@NC-mNS/NF, the electrocatalysts still maintained the dominant peaks of the Fe–Co–O/Co@NC/NF with a slight positive shift toward the higher 2θ values, perhaps due to the lattice compression and relaxation occurred during the in situ oxidation. Although the main peaks remained unchanged after the in situ oxidation, new peaks with relatively low intensity appeared at 2θ values of 22.27°, 39.03°, and 54.01°, which could be assigned to the (110), (111), and (211) planes of CoOOH (JCPDS-ICCD: 00-026-0480), respectively, implying that there was a slight phase transformation during the in situ electrochemical oxidation (Figure 3A). The P-XRD diffractograms of Co–MOF/NF, FeCo–PBA, and $Fe_xCo_{3-x}O_4$/NF are shown in Figure S3 (Supporting Information), confirming their respective phases, identical to our previous report.[9]

Further, Raman spectra of Fe–Co–O/Co@NC/NF and Fe–Co–O/Co@NC-mNS/NF showed dominant peaks at Raman shifts of 1348 and 1574 cm⁻¹, corresponding to the D and G
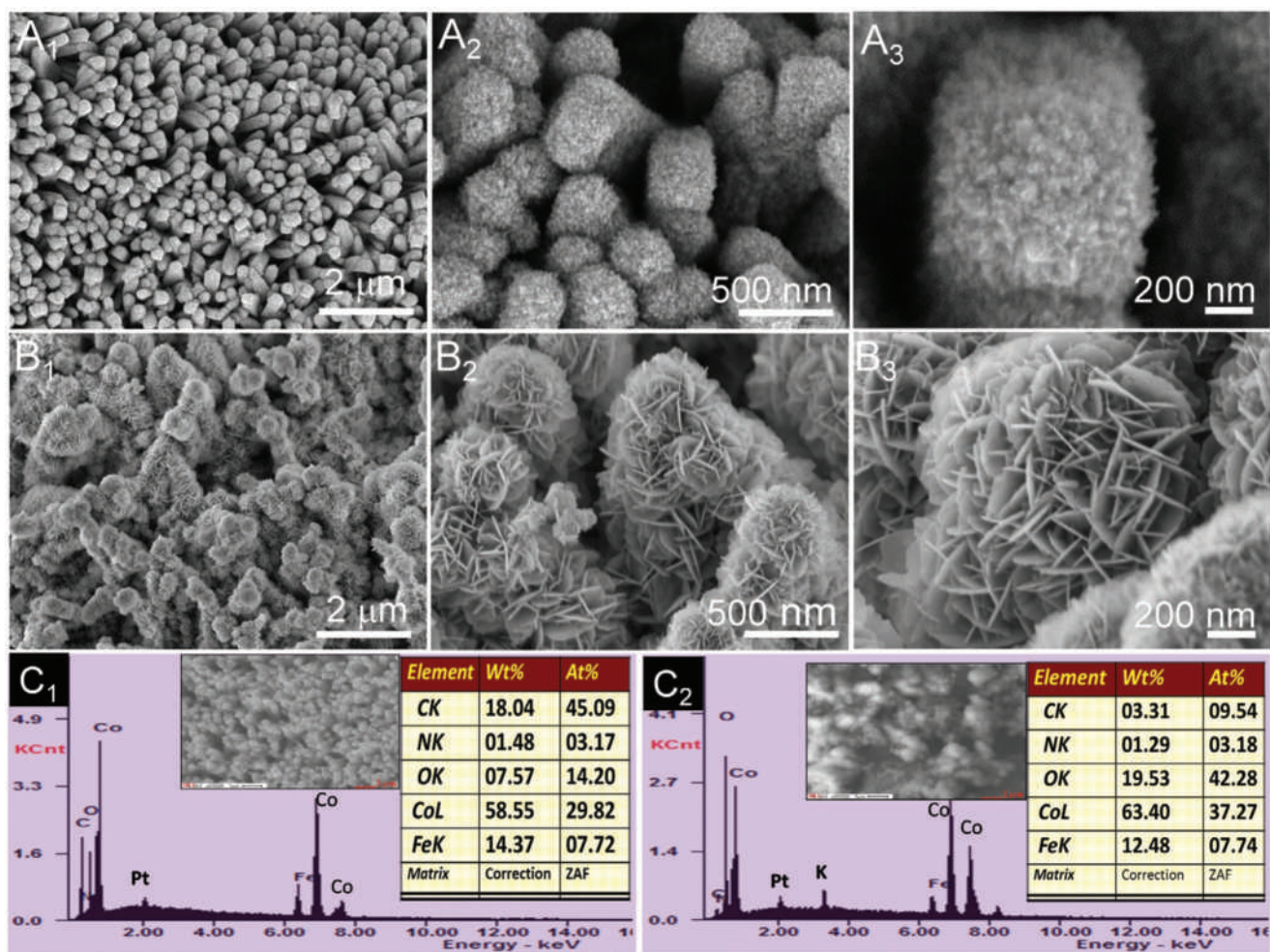
**ADVANCED
SCIENCE NEWS**
www.advancedsciencenews.com

NANO · MICRO
small
www.small-journal.com

Figure 2. Low- and high-magnification FE-SEM images and EDX spectra and elemental composition of A_1–A_3,C_1) Fe–Co–O/Co@NC/NF and B_1–B_3,C_2) in situ oxidized Fe–Co–O/Co@NC-mNS/NF.

bands, with an intensity ratio (I_D/I_G) = 1.1 and 1.3, respectively (Figure 2B). The higher I_D/I_G ratio may be assigned to the lattice defects induced by encapsulated metal/metal-oxide species and structural transformations during the in situ electrochemical oxidation. Further analysis of the Raman band below 1000 cm^{-1} showed that Fe–Co–O/Co@NC exhibited two dominant peaks at 470 and 650 cm^{-1} that can be assigned to E_g and A_{g1} vibrational modes of Co—O as observed in the defect rich CoO$_x$.[23–25] While in the case of the in situ oxidized Fe–Co–O/Co@NC-mNS, the corresponding E_g and A_{g1} peak positions were redshifted along with the generation of a broad band at ≈500–600 cm^{-1} corresponding to the vibrational modes of Co—O in CoOOH, indicating the formation of in situ oxidized metal (oxyhydr)oxide, in agreement with previous reports.[25–28] Further, the Brunauer–Emmett–Teller (BET) SSA calculation and Barrett–Joyner–Halenda (BJH) pore-size distribution analysis showed a typical type-IV adsorption isotherm curve with higher SSA (150 m^2 g^{-1}) (Figure 3C) and more mesoporous nature (Figure 3D) for Fe–Co–O/Co@NC-mNS/NF than those of Fe–Co–O/Co@NC/NF (SSA ≈ 110 m^2 g^{-1}). This confirms that the in situ morphological transformation resulted in high SSA and a mesoporous nature, corroborating the expectation from

FE-SEM observations, which would greatly facilitate the electrocatalytic activity by enabling a higher diffusion rate of reactants as well as the removal of evolved gases from the surface.

We also employed high-resolution transmission electron microscopy (HR-TEM) to further observe any internal structural changes caused by the in situ electrochemical oxidation. The Fe–Co–O/Co@NC/NF electrode showed a typical core–shell-like internal structure (**Figure 4**A_1,A_2), which resulted from the partial anion-exchange reaction during the formation of FeCo–PBA (Figure S4, Supporting Information). Under the heat treatment in an inert atmosphere, the metal centers were converted to either a metallic form or to oxides, while the nitrogen-containing organic parts became N-doped carbons.[29] Crystallite domains of metal nanoparticles/oxides were slightly agglomerated because of the high-temperature annealing but were uniformly dispersed over the N-doped carbon matrix (Figure 3A_1–A_4). Closer analysis of the lattice fringes (in regions 1 and 2 of Figure 4A_3) through fast Fourier transform (FFT) and the corresponding inverse fast Fourier transform (IFFT) (Figure 4A_5–A_8) showed an interplanar distance (d) of 0.21 nm corresponding to the (200) plane of CoO and 0.26 nm corresponding to (311) plane of Fe–Co–O, respectively, in agreement
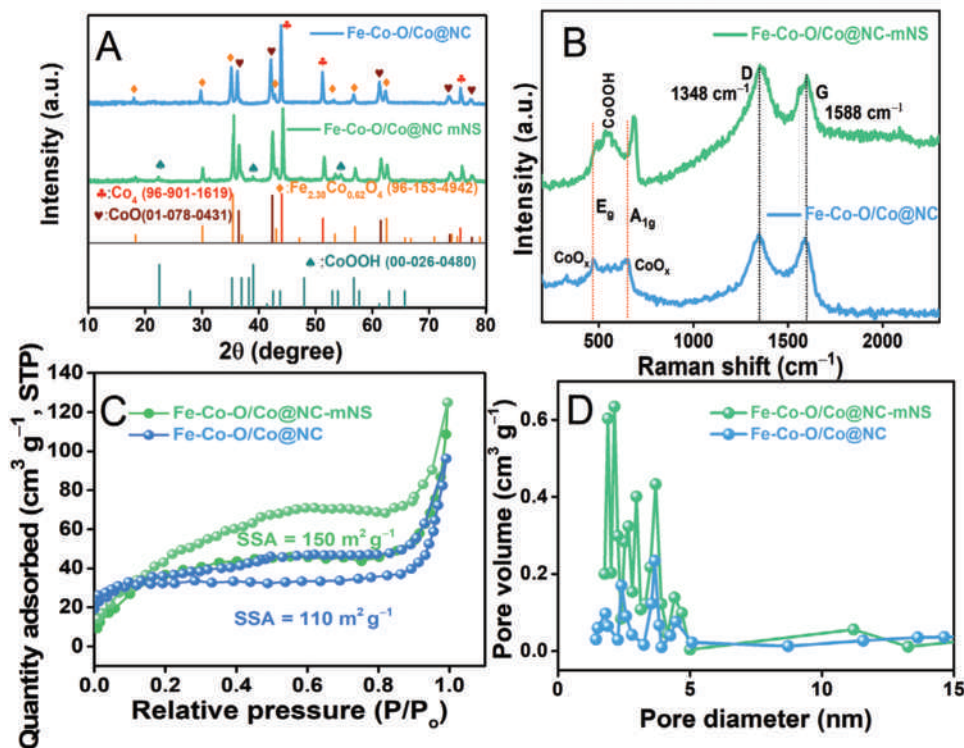
ADVANCED
SCIENCE NEWS
www.advancedsciencenews.com

NANO · MICRO
small
www.small-journal.com

Figure 3. A) Powder X-ray diffraction (P-XRD) patterns, B) Raman spectra, C) N_2 adsorption–desorption isotherm curves, and D) BJH pore-size distribution profiles of Fe–Co–O/Co@NC/NF and in situ oxidized Fe–Co–O/Co@NC-mNS/NF electrocatalysts.

with the P-XRD findings (Figure 2A). The N-doped carbon surrounding the metals was highly graphitized by the Co metals, thus encapsulating them by highly graphitic few-layered carbon shells (Figure $4A_4,A_9$). The FFT (Figure $4A_{10}$) and the corresponding IFFT (Figure $4A_{11}$) of region 3 of Figure $4A_4$ showed lattice fringes of 0.2 corresponding to the (111) plane of Co_4, in agreement with the P-XRD results. After the OER evaluation, TEM and HR-TEM analysis of the in situ oxidized Fe–Co–O/Co@NC-mNS/NF showed in situ developed internal structures. The granular crystallites observed in Fe–Co–O/Co@NC/NF (Figure $4A_2,A_3$) were greatly diminished (Figure $4B_1,B_2$). High-magnification HR-TEM images (regions 1 and 2 of Figure $4B_2$) showed the existence of various point defects and lattice distortions, which might have resulted from the in situ generated potential-dependent lattice stress and strain that evolved during the potential cycling of water oxidation evaluations.[21] The FFT (Figure $4B_5,B_7$) and the corresponding IFFT (Figure $4B_6,B_8$) of regions 3 and 4 of Figure $3B_2$ showed the lattice fringes of 0.24 nm corresponding to the (111) plane of the in situ oxidized CoOOH species, and 0.25 nm corresponding to the (311) plane of Fe–Co–O, as is consistent with the P-XRD results. The selected area under the diffraction (SAED) pattern of the in situ oxidized Fe–Co–O/Co@NC-mNS/NF showed more distinctly visible circular rings with bright dots, indicating that it was more crystallized than the Fe–Co–O/Co@NC/NF (Figure $4C_1,C_2$). Further, high-angle annular dark-field scanning transmission electron microscopy (HAADF-STEM) images and the elemental color mapping showed the presence of Co, Fe, O, N, and C and their spatial distributions (Figure $4C_3,C_4$). The

existence of more oxygen species in Fe–Co–O/Co@NC-mNS/NF than in Fe–Co–O/Co@NC/NF corroborates the in situ oxidation during the OER evaluations. However, other elements, such as Fe, N, and C, were lessened after the OER evaluations, which indicates that there might be a partial dissolution into the electrolyte during electrochemical evaluations, similar to the observations made in previous reports.[30–32]

Further, we employed X-ray photoelectron spectroscopy (XPS) to investigate the elemental compositions and near-surface chemical states of the constituent elements of the electrocatalysts before and after the OER evaluations (**Figure 5**). In general, under the harsh OER conditions, electrocatalysts usually undergo in situ electrochemical oxidation, resulting in physicochemical changes. The XPS survey spectrum in Figure 5A shows the presence of Co, Fe, O, N, and C as the main components of Fe–Co–O/Co@NC/NF before OER evaluations. After the OER evaluations, the XPS survey spectrum of the in situ oxidized Fe–Co–O/Co@NC-mNS/NF electrode showed similar compositions, except for N (Figure 5A). The absence of N in the survey spectrum of the in situ oxidized Fe–Co–O/Co@NC-mNS/NF electrodes may arise from the dissolution of N species from the surface of the electrocatalyst during the OER evaluation. Interestingly, the intensity of the O 1s peak was increased greatly after OER evaluation, indicating the occurrence of in situ electrochemical oxidation (Figure 5A). High-resolution Co 2p XPS spectra recorded before and after OER evaluations corroborated the in situ oxidation process (Figure 5B). Before OER evaluation, the Co 2p XPS spectrum showed spin–orbit duplets at binding energies of ≈780 and 796 eV, which
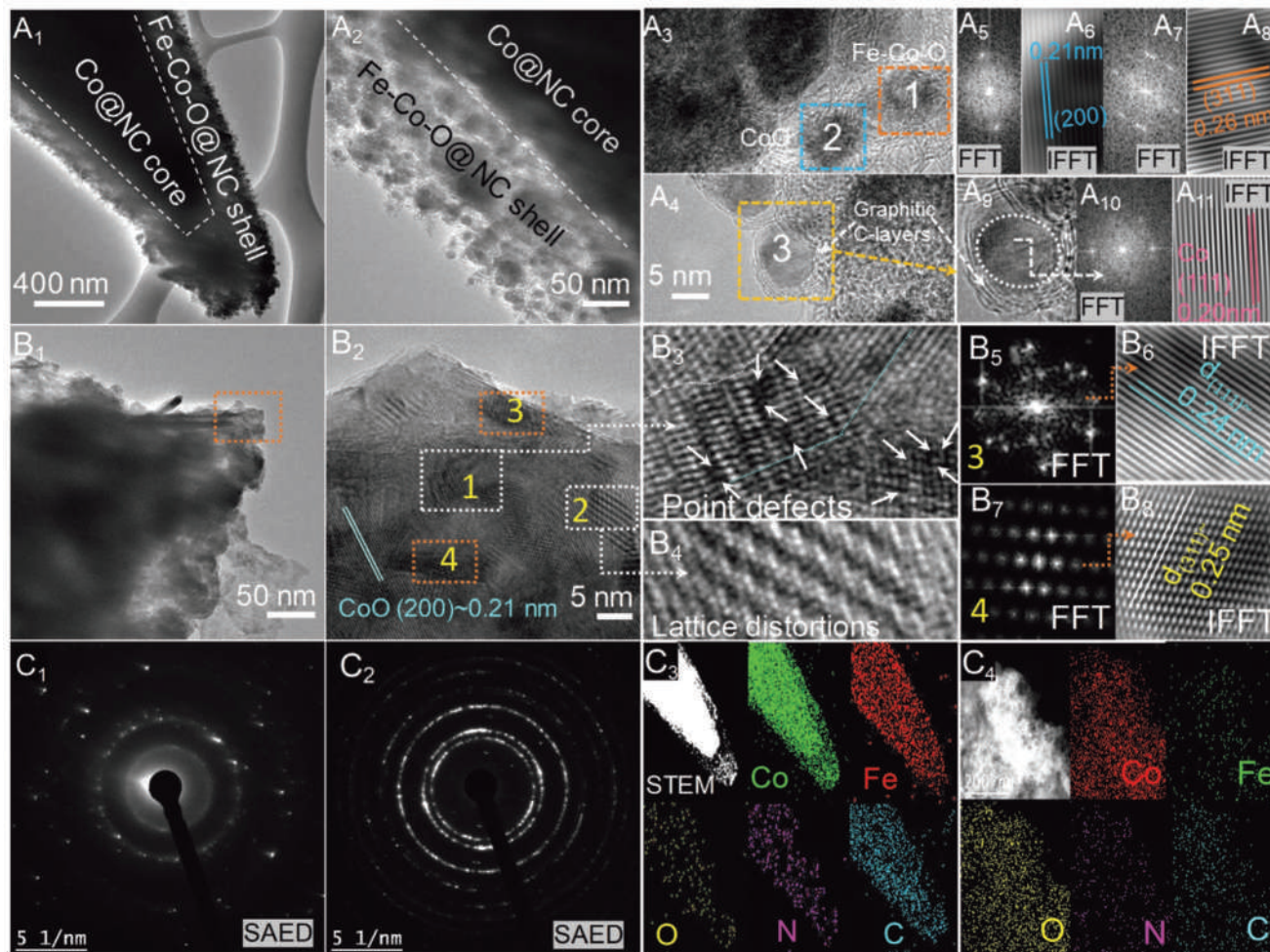
Figure 4. A₁,A₂) TEM, A₃,A₄) HR-TEM images, A₅–A₈) FFT and the corresponding IFFT of regions 2 and 1 of (A₃), A₉) magnified HR-TEM image of region 3 in A₄, A₁₀,A₁₁) FFT and the corresponding IFFT for Fe–Co–O/Co@NC/NF. B₁) TEM image, B₂) HR-TEM images, B₃,B₄) magnified HR-TEM images (regions 1 and 2 of (B₂)), B₅–B₈) FFT and the corresponding IFFT (regions 3 and 4 of (B₂)) of the in situ oxidized Fe–Co–O/Co@NC-mNS/ NF. C₁,C₂) SAED patterns and C₃,C₄) HAADF-STEM images and elemental color mappings of Fe–Co–O/Co@NC/NF and in situ oxidized Fe–Co–O/ Co@NC-mNS/NF.

are assigned to the Co $2p_{3/2}$ and Co $2p_{1/2}$ of $CoO_x@N-C$.[7,33] The deconvoluted peaks at 778.33 and 793.61 eV correspond to metallic Co.[33] The peaks at 780.57 and 796.88 eV can be attributed to the CoO phase.[7] The integration of the area under the deconvoluted curves showed the ratio of Co^{2+}/Co^{3+} to be 3.4, and metallic Co^0 occupied ≈25.4%. The presence of a higher Co^{2+}/Co^{3+} ratio is an indicator of oxygen vacancies that could arise from high-temperature annealing under an inert atmosphere.[34] The broad shoulder peaks at 784.99 and 803.26 eV are the satellite peaks of Co $2p_{3/2}$ and Co $2p_{1/2}$.[33] However, after OER evaluations, the Co^0 peak disappeared, and the Co^{3+} peak increased; so the Co^{2+}/Co^{3+} ratio was reduced to only 1.52, which indicates that the Co^0 species at the surface of the electrocatalysts underwent in situ oxidation to its corresponding oxyhydroxide, in consistent with the XRD observations. The lower value of the Co^{2+}/Co^{3+} ratio of Fe–Co–O/Co@NC-mNS/ NF indicates the presence of fewer oxygen vacancies than in the Fe–Co–O/Co@NC/NF electrocatalysts. However, in both cases, Co^{2+} is the dominant Co species in both materials. The O 1s

spectra also showed three deconvoluted peaks at the binding energies ≈529.59, 531.85, and 533.22 eV (Figure 5C). The peak at the binding energy of 529.59 eV is associated with oxygen atoms bonded to metal species, and the peak at 533.22 eV is due to the OH^- species of surface-adsorbed water molecules or C−OH bonds.[35] The dominant deconvoluted O 1s peak at 531.85 eV corresponds to abundant oxygen vacancies occurring at low oxygen coordinated defect sites.[35] After the OER evaluation, the deconvoluted peak corresponding to the M−O bond increased over that before OER evaluation, suggesting the in situ oxidation of the metal oxide to metal (oxyhydr) oxide, in agreement with the XRD results. Further to explain the role of the Fe species in the Co-based materials, the change in the valence state of Fe before and after the OER evaluation was investigated from the deconvoluted Fe 2p XPS spectra, as shown in Figure 5D. The Fe 2p XPS spectrum recorded before the OER evaluation showed peaks at the binding energies ≈710.8 and 724.4 eV corresponding to Fe $2p_{3/2}$ and Fe $2p_{1/2}$ of Fe_2O_3.[36,37] The peaks at the binding energies of 709.6 and
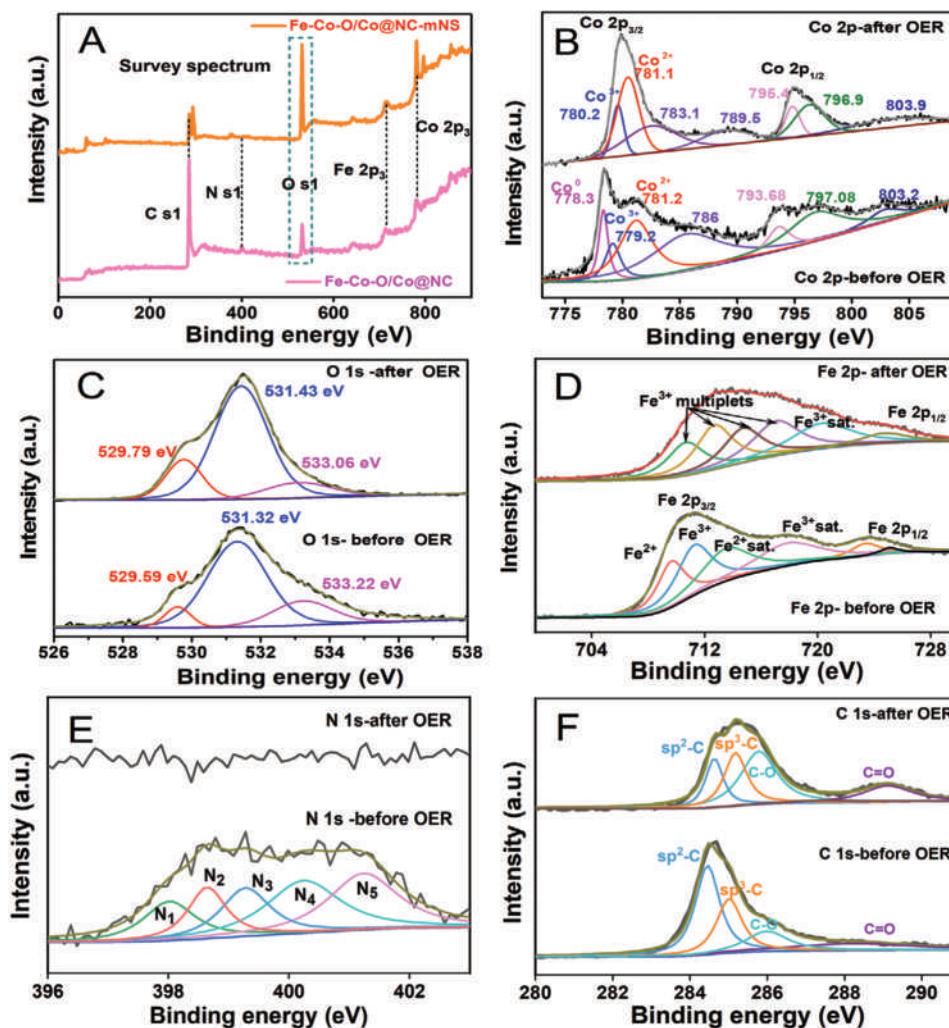
Figure 5. X-ray photoelectron spectra of Fe–Co–O/Co@NC/NF and in situ oxidized Fe–Co–O/Co@NC-mNS/NF electrocatalysts: A) survey spectrum, high-resolution spectra for B) Co 2p, C) O 1s, D) Fe 2p, E) N 1s, and F) C 1s.

711.3 eV correspond to Fe^{2+} and Fe^{3+}, while the peaks at the binding energies of 715.2 and 718.2 eV are the corresponding satellite peaks, in agreement with the previous reports.[37,38] However, Fe 2p XPS spectrum recorded after the OER evaluation (Figure 5D) showed a broad peak constituting four deconvoluted peaks corresponding to Fe^{3+} multiplets and a satellite peak, similar to surface oxidized iron oxides having abundant Fe^{3+} species, reported previously.[38] The presence of Fe^{3+} species can improve the properties of cobalt-based materials by promoting the Co^{2+} oxidation, charge-transfer kinetics, and electrochemical active surface area (ECSA), thereby enhancing the catalytic activities toward water oxidation.[39] Moreover, a previous density-function theory study also suggested that the presence of Fe^{3+} species can activate CoOOH lattice by inducing lower energy levels of the reaction intermediates and the products, resulting in higher OER performances.[40] Thus, in our case also, the presence of Fe^{3+} species can activate the in situ generated CoOOH species in Fe–Co–O/Co@NC-mNS/NF and is expected to show higher OER activities. Further, the XPS analysis of N 1s spectrum showed five deconvoluted peaks

represented as N_1, N_2, N_3, N_4, and N_5 at the binding energies of 398.1, 398.6, 399.3, 400.2, and 401.2 eV, respectively (Figure 5E), corresponding to pyridinic, pyrrolic, graphitic, pyridinic, and quaternary nitrogen species.[41,42] However, N 1s XPS spectrum after the OER did not show any peaks, indicating that the surface nitrogen species, which were present before the electrochemical evaluation, had completely disappeared after the in situ oxidation, perhaps because of the dissolution of the surface N species into the electrolyte. The deconvoluted high-resolution C 1s XPS spectrum also showed four peaks at the binding energies of 284.4, 285.0, 286.1, and 288.5 eV corresponding to those of sp^2-bonded carbon, the sp^3-bonded carbon, C—O, and C=O bonded species.[43] Further analysis of XPS spectra in the binding energy region of 291–997 eV (Figure S5, Supporting Information), showed two peaks at the binding energies of 293 and 295 eV corresponding to K $2p_{3/2}$ and K $2p_{1/2}$ of K 2p, respectively (Figure S5, Supporting Information), which are attributed to K remained on the surface after electrochemical evaluations in KOH electrolyte, in agreement with the occurrence of the peak around 3.5 keV in the EDX spectra (Figure 2C₂).[44]

ADVANCED
SCIENCE NEWS
www.advancedsciencenews.com

NANO · MICRO
small
www.small-journal.com

2.2. Electrochemical Characterization

2.2.1. Evaluations for OER

The detailed process of evaluating OER activities of the electrocatalysts is described in the Experimental Section. Since the redox reactions of oxides are often found to be overlapped with OER, the CV technique can provide useful information to distinguish the above two different reactions. The CV profiles of Fe–Co–O/Co@NC/NF and the in situ oxidized Fe–Co–O/Co@NC-mNS/NF evaluated in 1 M KOH electrolyte (Figure S6, Supporting Information) clearly demonstrated that the OER happened after the oxidation peaks occurring at potentials around 1.25–1.28 and 1.40–1.43 V (vs reversible hydrogen electrode (RHE)) corresponding to Co(II) $\leftrightarrow$ Co(III) $\leftrightarrow$ Co(IV), consistent

with previous reports.[45,46] The peaks corresponding to Co(II) $\leftrightarrow$ Co(III) $\leftrightarrow$ Co(IV) are not well distinguishable due to the presence of N-doped carbon matrix, and other microstructural effects,[46,47] however, it was clearly observed from the CV profiles that OER occurred after the redox peak positions (Figure S6, Supporting Information) and both the reactions can be differentiated easily. The difference in the peak potentials and redox peak currents of Fe–Co–O/Co@NC-mNS/NF and Fe–Co–O/Co@NC/NF are due to different surface morphologies, SSAs, spatial arrangements, and crystallite sizes in their nanosheets and micropillar structures.[46] Further, the OER performances of Fe–Co–O/Co@NC/NF, in situ oxidized Fe–Co–O/Co@NC-mNS/NF, Fe$_x$Co$_{3-x}$O$_4$/NF, RuO$_2$/NF, and bare NF are shown in **Figure 6**. Linear sweep voltammetry (LSV) profiles at the scan rate of 2 mV s^{-1} showed the best OER activity for the in situ oxidized sample,
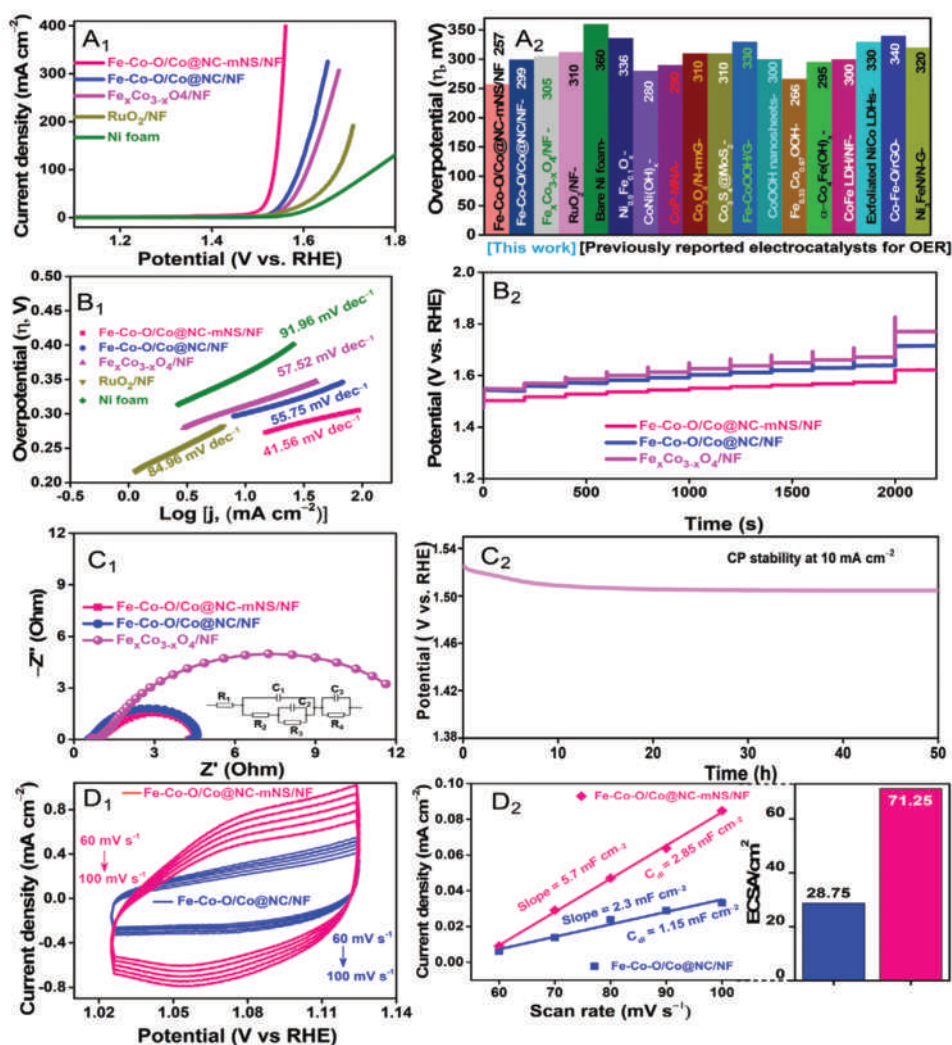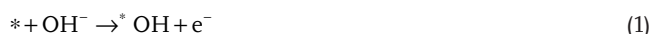

Figure 6. Evaluation for oxygen evolution reaction (OER): A$_1$) linear sweep voltammetry (LSV) curves, A$_2$) overpotential comparisons at 10 mA cm^{-2} of our prepared electrode materials (Fe–Co–O/Co@NC-mNS/NF, Fe–Co–O/Co@NC/NF, Fe$_x$Co$_{3-x}$O$_4$/NF with RuO$_2$/NF and bare Ni foam) with various other recently reported OER electrocatalysts: Ni$_{0.9}$Fe$_{0.1}$O$_x$,[49] CoNi(OH)$_x$,[50] CoP–MNA (MNA: mesoporous nanorod arrays),[51] Co$_3$O$_4$/N-rmG (rmG: reduced mildly oxidized graphene),[52] Co$_3$S$_4$@MoS$_2$,[53] Fe–CoOOH/G,[54] CoOOH nanosheets,[55] Fe$_{0.33}$Co$_{0.67}$OOH,[40] α-Co$_4$Fe(OH)$_x$,[56] CoFe–LDH/NF,[57] exfoliated NiCo–LDH,[58] Co–Fe–O/rGO,[59] Ni$_3$FeN/N–G,[60] etc. B$_1$) Tafel plots, B$_2$) multistep current profiles, C$_1$) EIS profiles, and C$_2$) chronopotentiometry (CP) long-term stability test at current density of 10 mA cm^{-2} for 50 h. D$_1$) CV profiles of Fe–Co–O/Co@NC-mNS/NF and Fe–Co–O/Co@NC/NF at different scan rates (60–100 mV s^{-1}) and D$_2$) determination of C$_{dl}$ from the graph of current density versus scan rates and the corresponding calculated ECSA values.

**ADVANCED
SCIENCE NEWS**
www.advancedsciencenews.com

**NANO · MICRO
small**
www.small-journal.com

Fe–Co–O/Co@NC-mNS/NF, demonstrating a very low overpotential of 257 mV at the current density of 10 mA cm^{-2} compared to Fe–Co–O/Co@NC/NF (299 mV), Fe$_x$Co$_{3-x}$O$_4$/NF (305 mV), RuO$_2$/NF (301 mV), bare Ni foam (360 mV) (Figure 6A$_1$). Fe–Co–O/Co@NC-mNS/NF further demonstrated high efficiency by demanding extremely low overpotentials of 305 and 330 mV even at high current densities of 100 and 400 mA cm^{-2}. At all the current densities, the OER performance is in the order of Fe–Co–O/Co@NC-mNS/NF > Fe–Co–O/Co@NC/NF > Fe$_x$Co$_{3-x}$O$_4$/NF > RuO$_2$/NF > bare NF. Further to examine the effect of Fe incorporation on cobalt-based materials toward the OER activities, we have also evaluated the OER activity of the pristine-Co–MOF/NF-derived Co@NC/NF under the same condition. The LSV profile of Co@NC/NF in comparison to those of Fe–Co–O/Co@NC-mNS/NF, Fe–Co–O/Co@NC/NF, and Fe$_x$Co$_{3-x}$O$_4$/NF is shown in Figure S7 (Supporting Information). The pristine-Co–MOF/NF-derived Co@NC/NF showed much higher overpotentials at all current densities compared to those of Fe-incorporated Co-based materials (Figure S7, Supporting Information) which signifies that the Fe incorporation indeed enhances the OER activities of the Co-based electrocatalysts, in agreement to previous reports.[48] The overpotential of our best electrocatalyst, Fe–Co–O/Co@NC-mNS/NF, is superior to that of the various types of recently reported electrocatalysts, such as layered double hydroxides (LDHs), sulfides, phosphides, nitrides, and carbides (Figure 6A$_2$ and Table S1 (Supporting Information)). Such superior electrochemical performance of the electrocatalysts over the pre-existing materials is rarely reported. We also investigated the electrochemical kinetics of the electrocatalysts from the Tafel plots, which showed a Tafel slope of 41.56 mV dec^{-1} for the in situ oxidized Fe–Co–O/Co@NC-mNS/NF, which is less than those of Fe–Co–O/Co@NC/NF (68.62 mV dec^{-1}), Fe$_x$Co$_{3-x}$O$_4$/NF (57.52 mV dec^{-1}), RuO$_2$/NF (84.96 mV dec^{-1}), and Ni foam (91.96 mV dec^{-1}) (Figure 6B$_1$). Multistep potential profiles also corroborate that the in situ oxidized Fe–Co–O/Co@NC-mNS/NF (Figure 6B$_2$) works better than Fe–Co–O/Co@NC/NF and Fe$_x$Co$_{3-x}$O$_4$/NF. The OER activity at an active site (*) in an alkaline solution is generally assumed to begin with a proton-coupled electron transfer from aquo species bonded at the metal surface followed by O—O bond formation, schematically represented as follows[4]

$$* + OH^- \rightarrow \,^* OH + e^- \tag{1}$$

$$^*OH + OH^- \rightarrow \,^* O + H_2O + e^- \tag{2}$$

$$^*O + OH^- \rightarrow \,^* OOH + e^- \tag{3}$$

$$^*OOH + OH^- \rightarrow \,^* O_2 + e^- \tag{4}$$

$$^*O_2 \rightarrow * + O_2 \tag{5}$$

Further, the Nyquist plot fitted with the corresponding equivalent circuit diagram showed higher electrical conductivity and faster charge transportability for the in situ oxidized Fe–Co–O/Co@NC-mNS/NF sample (Figure 6C$_1$), as indicated by the lower electrochemical series resistance and smaller semicircular region representing charge-transfer resistance (R_{ct}), compared to that of Fe–Co–O/Co@NC/NF and Fe$_x$Co$_{3-x}$O$_4$/NF, in agreement with findings from Tafel plots, LSV, and multistep profiles. Thus, we observed that the in situ oxidized Fe–Co–O/Co@NC-mNS/NF sample showed the best OER activity in terms of overpotential. The long-term stability evaluation using the chronopotentiometry (CP) technique at a current density of 10 mA cm^{-2} for 50 h showed that the overpotential dropped in the initial few hours of the test, but later on stayed constant for up to 50 h (Figure 6C$_2$), similar to previous reports.[61] The decrease in the overpotential was attributed to the activation of Co^{2+} sites by the Fe species during the electrochemical evaluations for OER, in agreement with previous reports.[39] This corroborates that the Fe–Co–O/Co@NC/NF underwent in situ electrochemical oxidation to form Fe–Co–O/Co@NC-mNS/NF, as is evident from the XRD, FE-SEM, TEM, and XPS studies. Further, the LSV profile recorded after the long-term stability test of 1000 CV cycles of the in situ oxidized Fe–Co–O/Co@NC-mNS/NF electrocatalyst showed negligible deterioration, signifying its high electrocatalytic stability (Figure S8, Supporting Information). The morphology of the in situ oxidized Fe–Co–O/Co@NC-mNS/NF electrocatalyst after the 1000 CV cycles was also investigated by FE-SEM and found to exhibit almost the same mesoporous nanosheet structures, indicating high stability (Figure S9, Supporting Information). To investigate the higher performance of the in situ oxidized Fe–Co–O/Co@NC-mNS/NF compared to that of Fe–Co–O/Co@NC/NF, we evaluated the ECSA of both materials under the same potential range as a function of various scan rates (Figure 6D$_1$,D$_2$), which showed a higher ECSA (71.25 cm^{-2}) for the in situ oxidized Fe–Co–O/Co@NC-mNS/NF than for the Fe–Co–O/Co@NC/NF (28.75 cm^{-2}). Such an increase in the ECSA could have resulted due to more exposed active sites of the in situ generated metal (oxyhydr)oxides in the nanosheet structure of the oxidized Fe–Co–O/Co@NC-mNS/NF than in the bulk Fe–Co–O/Co@NC/NF micropillars. Thus, high OER performance of the in situ oxidized Fe–Co–O/Co@NC-mNS/NF can be attributed to in situ morphological transformation, resulting in high SSA nanosheets, higher ECSA, and the optimum oxygen vacancies generated during the OER evaluations.

2.2.2. Evaluations for HER

We measured the HER activity of the prepared samples, Fe–Co–O/Co@NC-mNS/NF, Fe–Co–O/Co@NC/NF, and Fe$_x$Co$_{3-x}$O$_4$/NF, along with Pt/C/NF and bare NF for comparison, using a three-electrode configuration in 1 m KOH electrolyte. The LSV profiles of the electrocatalysts recorded at a low scan rate of 2 mV s^{-1} are shown in **Figure 7**A. Among the prepared electrocatalysts, Fe–Co–O/Co@NC-mNS/NF showed a lower overpotential of 112 mV, compared to those of Fe–Co–O/Co@NC/NF (141 mV) and Fe$_x$Co$_{3-x}$O$_4$/NF (194 mV), whereas Pt/C/NF and NF showed overpotentials of 10 and 307 mV, respectively, to generate a current density of 10 mA cm^{-2}. Even at the high current density of 100 mA cm^{-2}, Fe–Co–O/Co@NC-mNS/NF showed a very low overpotential of 201 mV, whereas Fe–Co–O/Co@NC/NF and Fe$_x$Co$_{3-x}$O$_4$/NF demand higher overpotentials of 237 and 353 mV, respectively. The
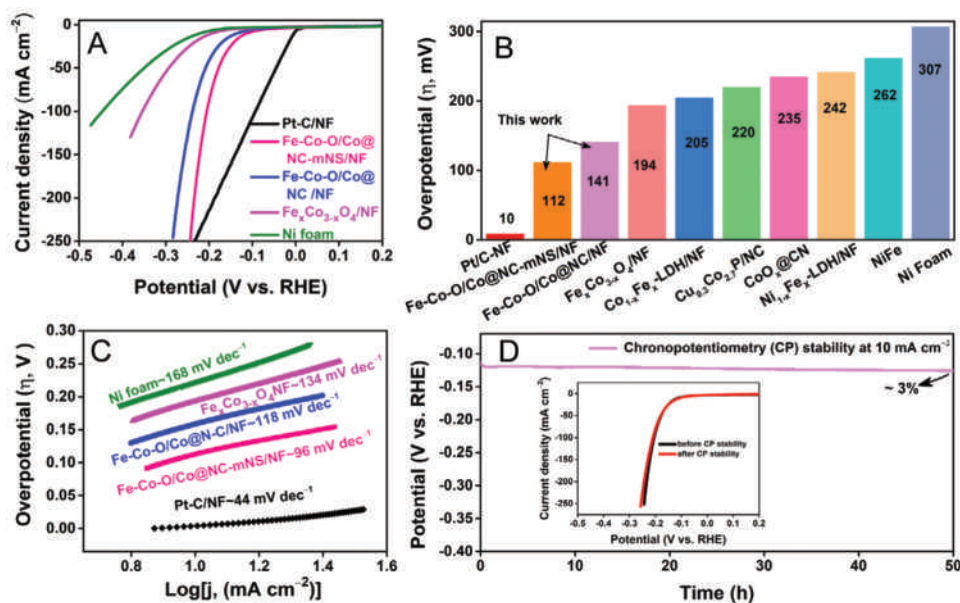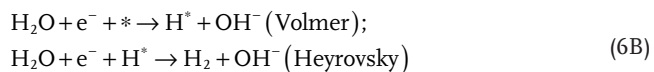
Figure 7. A) iR-corrected LSV profiles at the scan rate of 2 mV s^{-1} of Fe–Co–O/Co@NC-mNS/NF, Fe–Co–O/Co@NC/NF, Fe$_x$Co$_{3-x}$O$_4$/NF, Pt–C/NF, and Ni foam, B) overpotential at the current density of 10 mA cm^{-2} compared with previously reported electrocatalysts, such as Co$_{1-x}$Fe$_x$–LDH/NF,[62] Cu$_{0.3}$Co$_{2.7}$P/NC,[63] CoO$_x$@CN,[7] Ni$_{1-x}$Fe$_x$–LDH/NF,[62] and NiFe,[64] C) Tafel plots, and D) long-term chronopotentiometry stability test for Fe–Co–O/Co@NC-mNS/NF electrocatalysts at the current density of 10 mA cm^{-2} for 50 h.

overpotential of bare Ni foam substrate which is larger than that of the prepared electrocatalysts implies that the high electrocatalytic activity resulted from the active materials and not from the Ni foam substrate. In addition, Fe–Co–O/Co@NC-mNS/NF also showed a lower overpotential compared to some recently reported HER electrocatalysts, such as Co$_{1-x}$Fe$_x$–LDH/NF,[62] Cu$_{0.3}$Co$_{2.7}$P/NC,[63] CoO$_x$@CN,[7] Ni$_{1-x}$Fe$_x$–LDH/NF,[62] and NiFe,[64] indicating its excellent HER activity (Figure 7B). To further investigate the HER kinetics of the electrocatalysts, we derived the Tafel plot from the iR-corrected LSV profiles, as shown in Figure 7C. The obtained Tafel slopes of the prepared electrocatalyst were in the order Pt/C/NF (44 mV dec^{-1}) < Fe–Co–O/Co@NC-mNS/NF (96 mV dec^{-1}) < Fe–Co–O/Co@NC/NF (118 mV dec^{-1}) < Fe$_x$Co$_{3-x}$O$_4$/NF (134 mV dec^{-1}) < Ni foam (168 mV dec^{-1}). This showed that the Fe–Co–O/Co@NC-mNS/NF electrocatalyst showed higher HER kinetics compared to that of Fe–Co–O/Co@NC/NF, Fe$_x$Co$_{3-x}$O$_4$/NF, and various other recent HER electrocatalysts (Table S2, Supporting Information). The HER process in principle can proceed following either a Volmer–Tafel mechanism (Equation (6A)) or a Volmer–Heyrovsky pathway (Equation (6B)) in an alkaline medium, as represented below[7]

$$H_2O + e^- + * \rightarrow H^* + OH^- \,(\text{Volmer}); H^* + H^* \rightarrow H_2 \,(\text{Tafel}) \quad (6A)$$

$$\begin{aligned} &H_2O + e^- + * \rightarrow H^* + OH^- \,(\text{Volmer}); \\ &H_2O + e^- + H^* \rightarrow H_2 + OH^- \,(\text{Heyrovsky}) \end{aligned} \quad (6B)$$

where * represents an active site. In both mechanisms, there is adsorption of H$_2$O at the active site and then dissociation of the adsorbed H$_2$O into adsorbed H atoms (H*) and OH$^-$, followed by the desorption of OH$^-$ again to refresh the surface

and transform the adsorbed H atoms into H$_2$ gaseous molecule. Although the exact mechanism for HER in alkaline media is still not fully clarified, the Tafel slopes of Fe–Co–O/Co@NC-mNS/NF (96 mV dec^{-1}) and Fe–Co–O/Co@NC/NF (118 mV dec^{-1}) suggest that HER activities of these electrocatalysts obeyed a Volmer–Heyrovsky mechanism represented in Equation (6B).[65] Previous studies show that Co has suitable binding energy for the H atom,[6] close to that of Pt, whereas its oxides, such as CoO and Co$_3$O$_4$, can undergo hydroxylation to dissociate water molecules.[66] Therefore, the presence of Co^{+2} and Co^{+3} states in our Fe–Co–O/Co@NC-mNS/NF and Fe–Co–O/Co@NC/NF electrocatalysts can preferentially attract OH$^-$ generated during the water dissociation on their surface because of their strong electrostatic force of attraction for being positively charged, whereas the cobalt (Co^0) sites in the neighborhood can facilitate the Volmer process by increasing the adsorption of H and providing the synergistic effect to CoO during HER.[7] Moreover, the higher SSA and porous nature resulting from thin and interconnected mesoporous nanosheet structures of the in situ oxidized Fe–Co–O/Co@NC-mNS/NF electrocatalyst (Figures 2A,B and 3C) can facilitate higher electrode–electrolyte interactions, enabling higher charge-transfer kinetics for Fe–Co–O/Co@NC-mNS/NF compared to Fe–Co–O/Co@NC/NF which accounts for the higher HER activity.[67] In addition, the electrochemical impedance spectroscopy (EIS) measurement during HER demonstrated a smaller semicircular region for the mesoporous nanosheets of Fe–Co–O/Co@NC-mNS/NF, indicating its lower charge transfer resistance (R_{ct}) compared to that of the bulky Fe–Co–O/Co@NC/NF micropillar arrays, as shown in Figure S10 (Supporting Information). In principle, an ideal HER electrocatalyst is assumed to follow the Brønsted–Evans–Polanyi principle, and OH$^-$ adsorption affinity of the oxophilic groups should be optimum; that is, it should be neither

**ADVANCED
SCIENCE NEWS**

www.advancedsciencenews.com

**NANO · MICRO
small**

www.small-journal.com

too strong, to avoid surface poisoning, nor too weak to cause binding, in order to facilitate the HER kinetics.[65] Moreover, the long-term stability of the electrocatalysts is greatly important for practical applications. So, we evaluated the long-term stability of our best-performing Fe–Co–O/Co@NC-mNS/NF electrode using a CP test at an applied current density of 10 mA cm^{-2} for 50 h, shown in Figure 7D. After the CP stability test for 50 h, the Fe–Co–O/Co@NC-mNS/NF electrode showed only a 3% increase in the overpotential over that of the initial value, indicating its robust long-term electrochemical stability. Further, the LSV profiles recorded after the CP stability test showed a very small change compared to that before the CP stability, as shown in the inset of Figure 7D. Thus, Fe–Co–O/Co@NC-mNS/NF demonstrated excellent HER activities besides its promising OER performances, signifying its bifunctional electrocatalytic properties.

2.2.3. Evaluations for Overall Water Splitting

We also examined the overall water-splitting ability of the prepared electrocatalysts by using the various prepared materials, Fe–Co–O/Co@NC-mNS/NF, Fe–Co–O/Co@NC/NF, and Fe$_x$Co$_{3-x}$O$_4$/NF, as anode and cathode in various combinations. We assembled four different electrolyzers [Fe–Co–O/Co@NC-mNS/NF (+/−); Fe–Co–O/Co@NC-mNS/NF (+); Fe–Co–O/Co@NC/NF (−); Fe–Co–O/Co@NC/NF (+/−); and Fe$_x$Co$_{3-x}$O$_4$/NF (+/−)] to find the most efficient electrolyzer. The state-of-the-art electrolyzers consisting of RuO$_2$ as anode and Pt/C as a cathode, as well as only bare Ni foam as both anode

and cathode, were also fabricated for comparative study. At a current density of 10 mA cm^{-2}, the electrolyzer consisting of Fe–Co–O/Co@NC-mNS/NF as both anode and cathode showed the lowest cell potential of 1.58 V next to the state-of-the-art electrolyzer consisting of RuO$_2$/NF (+) and Pt/C/NF (−), which required 1.56 V for the same current density (**Figure 8**A,B), whereas the electrolyzer consisting of Fe–Co–O/Co@NC-mNS/NF as anode and Fe–Co–O/Co@NC/NF as cathode required 1.59 V, which was slightly lower than the 1.62 and 1.66 V required for Fe–Co–O/Co@NC/NF (+/−) and Fe$_x$Co$_{3-x}$O$_4$/NF (+/−) electrolyzers at the same current density. These results show that the in situ oxidized Fe–Co–O/Co@NC-mNS/NF can function effectively as both anode and cathode materials and is highly effective in reducing the overall water-splitting cell potentials (Figure 8B). The cell potential for the overall water-splitting performance of the electrolyzers at the current density of 10 mA cm^{-2} followed the order: RuO$_2$/NF (+)//Pt/C/NF (−) < Fe–Co–O/Co@NC-mNS/NF (+/−) < Fe–Co–O/Co@NC-mNS/NF (+)//Fe–Co–O/Co@NC/NF (−) < Fe–Co–O/Co@NC/NF (+/−) < Fe$_x$Co$_{3-x}$O$_4$/NF (+/−) < Ni foam (+/−). However, at the high current density of 50 mA cm^{-2}, the Fe–Co–O/Co@NC-mNS/NF (+/−) electrolyzers surpassed the RuO$_2$/NF (+)//Pt/C/NF (−) electrolyzer and demanded only a low cell potential of 1.70 V, which is 30 mV less than that of the RuO$_2$/NF (+)//Pt/C/NF (−) electrolyzer (1.73 V) at the same current density. This showed that using the in situ oxidized Fe–Co–O/Co@NC-mNS/NF electrode as both anode and cathode is highly efficient for reducing the cell potential, and the fabricated electrolyzers showed better overall water-splitting performance
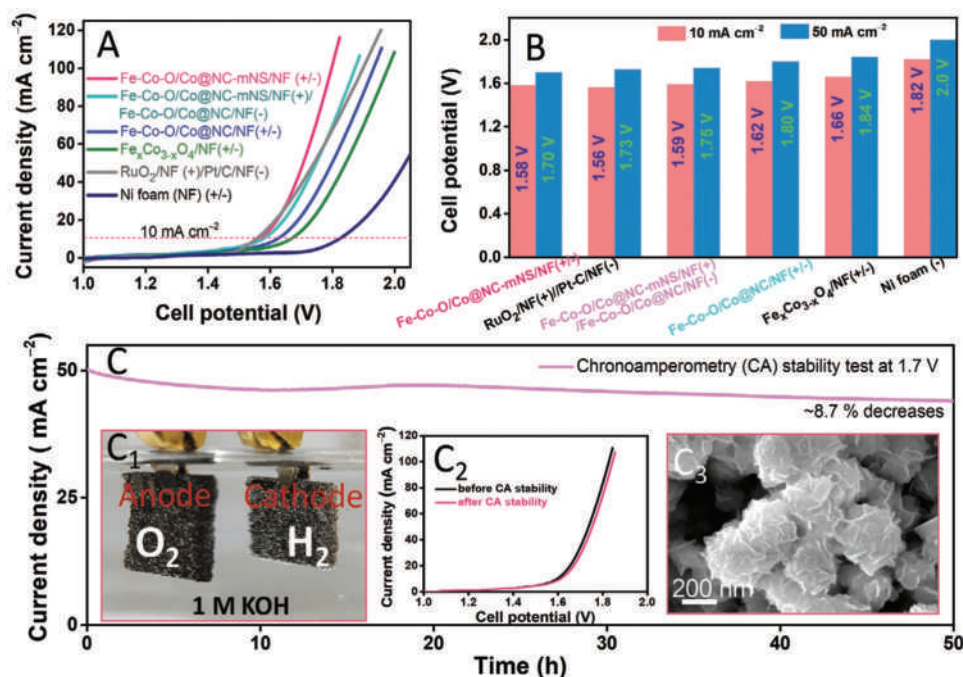

Figure 8. A) LSV profiles, B) cell potentials at the current density of 10 mA cm^{-2} of the alkaline electrolyzers: Fe–Co–O/Co@NC-mNS/NF (+/−); Fe–Co–O/Co@NC-mNS/NF (+)//Fe–Co–O/Co@NC/NF (−); Fe–Co–O/Co@NC/NF (+/−); Fe$_x$Co$_{3-x}$O$_4$/NF (+/−), RuO$_2$/NF (+)//Pt/C/NF (−); and bare Ni foam (+/−). C) Long-term chronoamperometric stability test at 1.7 V for 50 h. Insets: C$_1$) digital photographic image of Fe–Co–O/Co@NC-mNS/NF (+/−) electrolyzer, showing the evolution of O$_2$ and H$_2$ at the anode and cathode, respectively; C$_2$) LSV profile of Fe–Co–O/Co@NC-mNS/NF (+/−) electrolyzer before and after the CA stability test, showing a very small change; and C$_3$) FE-SEM images of the Fe–Co–O/Co@NC-mNS/NF electrode after the long-term CA stability test of the assembled electrolyzer.

than various recently reported electrolyzers (Table S3, Supporting Information).

Further, the long-term stability of the best electrolyzer, Fe–Co–O/Co@NC-mNS/NF (+/–) was also evaluated using chronoamperometric (CA) stability test conducted at an applied cell potential of 1.7 V. The Fe–Co–O/Co@NC-mNS/NF (+/–) electrolyzer exhibited high stability with only a small degradation of 8.7% of the initial current density over 50 h under the same applied cell potential (Figure 8C). The evolution of H_2 at the cathode and O_2 at the anode during the operation of Fe–Co–O/Co@NC-mNS/NF (+/–) electrolyzer is shown in Figure 8C$_1$, which demonstrates that the gas bubbles can be effectively dispatched from the electrode surface because of the high porosity of the electrodes; no large accumulation of gas bubbles occurred on the electrode's surface. The LSV profiles measured after the long-term CA stability showed a minute cell potential difference from the initial one, suggesting the long-term high stability of Fe–Co–O/Co@NC-mNS/NF electrocatalyst. Besides, the investigation of the morphological changes of the electrocatalysts after the long-term CA stability test showed that the mesoporous nanosheet structure was still maintained even after the stability test, indicating the robust morphological stability of the electrocatalyst as well (FE-SEM images in Figure 8C$_3$). Thus, the electrochemical evaluations for OER, HER, and the overall water splitting suggested that the developed electrodes and their synthesis strategy are highly promising for developing hybrid electrocatalysts, enabling low-potential alkaline electrolyzers for generating clean H_2 as a fuel for future generations.

3. Conclusion

In summary, we have developed a metal–organic-framework-derived defect-rich N-doped carbon-encapsulated Fe–Co–O/Co hybrid heterostructures on Ni foam as highly efficient pre-electrocatalysts using FeCo–PBA as a self-sacrificing template under annealing in Ar atmosphere. The developed Fe–Co–O/Co@NC/NF hybrid heterostructured electrocatalysts were rich in oxygen vacancies and underwent in situ electrochemical oxidation during the OER evaluation resulting to morphological changes from micropillar-like structure to uniform, thin, large, and mesoporous nanosheets. The newly evolved Fe–Co–O/Co@NC-mNS/NF electrocatalysts, because of their very thin and mesoporous nanosheet structures and higher SSA, showed higher ECSA. Accordingly, the in situ oxidized Fe–Co–O/Co@NC-mNS/NF showed much better OER, HER, and overall water-splitting performance than the Fe–Co–O/Co@NC/NF and $Fe_xCo_{3-x}O_4$/NF. The better performance of the in situ oxidized Fe–Co–O/Co@NC-mNS/NF electrode over others was attributed to 1) the higher SSA and mesoporous nature, which increased the available electrocatalyst's surface for interactions with the electrolyte, 2) higher ECSA and thin nanosheet structure, which exposed larger active sites for adsorption and desorption of the OER and HER intermediates, 3) presence of higher Co^{3+} oxidation states and suitable oxygen vacancies during the in situ oxidations along with the generation of highly active new metal-(oxyhydr)oxide phases. Thus, our study reveals the in situ electrochemical generation of Fe–Co–O/Co@NC-mNS/NF as more active electrocatalysts of

mesoporous nanosheets with defective sites and oxygen vacancies efficient for OER, HER, and overall water splitting. Thus, our design and synthesis of electrocatalysts with nanohybrid heterostructure using MOFs as precursor materials are highly beneficial for developing low-cost and highly effective electrocatalysts for various other energy-conversion applications.

4. Experimental Section

Chemicals: Cobalt nitrate hexahydrate, potassium hexacyanoferrate ($K_3[Fe(CN)_6]$), 2-methylimidazole, deionized (DI) water, potassium hydroxide, NF (99.9% Ni percentage, 98% porosity, 0.2–0.5 mm pore size, density ≈ 380 g m^{-2} ± 20, thickness ≈ 1.5 mm, length 250 mm) were from Taiyuan Liyuan Lithium Technology Co., Ltd., China).

Synthesis of Co–MOF/NF: The synthesis procedure of Co–MOF/NF was similar to that in the previous report with slight modifications.[9] Initially, cobalt nitrate hexahydrate (1 mmol) and 2-methylimidazole (16 mmol) were separately dissolved in 40 mL of DI water, then they were mixed under magnetic stirring for 1 min, and the precleaned Ni foam (two pieces of 2 × 4 cm^2 area) was submerged into the solution for 12 h. The gas bubbles on the Ni foam, if any developed, were properly dispersed. Finally, the Co–MOF/NF was collected, washed with DI water, and dried in an oven at 60 °C for 12 h.

Synthesis of FeCo–PBA/NF: The synthesis procedure for FeCo–PBA/NF was similar to that in the previous report with slight modifications.[9] Typically, Co–MOF/NF (two pieces of 2 × 4 cm^2) was immersed in a beaker with 50 mL of the aqueous solution of 0.5 mmol of $K_3[Fe(CN)_6]$ for 12 h at room temperature (25 °C). Finally, the Ni foams were collected and washed with DI water and dried at 60 °C.

Synthesis of Fe–Co–O/Co@NC/NF: Fe–Co–O/Co@NC/NF was synthesized by carbonization of FeCo–PBA/NF in an argon atmosphere using a two-step heating method. Typically, a quartz boat containing a piece of FeCo–PBA/NF was placed inside the furnace tube in an inert gas atmosphere maintained by flowing 500 sccm of Ar. The temperature was initially raised to 550 °C at a prolonged heating rate of 2.5 °C min^{-1} and maintained at the same temperature for 1 h, then the temperature was further increased to 800 °C and kept for 2 h. Finally, the heating was stopped and was allowed to cool down to room temperature. The mass loading of the electrocatalyst over 1 cm^2 was around 2 mg.

For comparison, a mixed oxide $Fe_xCo_{3-x}O_4$/NF electrocatalyst was also developed by simply heating the same FeCo–PBA/NF in the air at 400 °C for 2 h at the slow heating rate of 1 ° min^{-1}, as in the previous report.[9]

For comparison, pristine-Co–MOF/NF-derived Co@NC/NF was also synthesized under the same carbonization condition as that of Fe–Co–O/Co@NC/NF by using one piece of Co–MOF/NF instead of FeCo–PBA/NF.

Electrochemical Measurements: Evaluations in Three-Electrode and Two-Electrode Configurations: LSV, CV, and EIS were employed in the three-electrode configuration using a CHI 660E, US electrochemical workstation. All EIS measurements of the electrodes were done in the frequency range of 1^{-2}–10^5 Hz with a voltage amplitude of 5 mV. The EIS fitting of the equivalent impedance circuit diagrams was done using CHI 660E system software. The freshly prepared 1 M KOH aqueous solution was used as the working electrolyte, 1 cm^2 of the prepared materials as the working electrode, a graphite rod as the counter electrode, and Ag/AgCl (sat.) as the reference electrode during the entire electrochemical evaluation. The electrode materials were initially subjected to continuous 100 CV cycles at the scan rate of 20 mV s^{-1} for stabilization and then used for further electrochemical measurements in fresh electrolytes. The employed 100 CV cycles were also found to be sufficient for the structural transformation caused during the continuous voltage sweeps under CV.[20,61,68]

ECSA was calculated using the following equation[69]

$$ECSA = \frac{C_{dl}}{C_s} \tag{7}$$

where C_{dl} is the capacitance calculated from the non-Faradaic region and C_s is the specific capacitance of a flat, smooth electrode surface, numerically taken as 40 µF cm^{-2}.[69] For the calculation of C_{dl}, cyclic voltammograms of the electrode material in the non-Faradaic region were recorded at various scan rates, a graph of scan rates versus current densities ($\Delta j = j_{anodic} - j_{cathodic}$) was plotted, and the slope of the graph was calculated through the linear fitting. The value of the slope was numerically equal to twice the C_{dl} value, which was therefore half the slope value. Having found the C_{dl} and C_s values, ECSA was calculated using the above equation.

Material Characterizations: X-ray diffraction (Rigaku Corporation, Japan, CuKa radiation, wavelength = 0.154 nm) was to investigate the crystallinity and phase of the prepared materials by powder in the 2θ range of 10°–80° at a scan rate of 3° min^{-1}. FE-SEM (JSM-6701F; JEOL, Japan), energy-dispersive X-ray spectroscopy (SUPRA 40 VP, Carl Zeiss, Germany), and TEM (JEM-2200 FS, JEOL, Ltd., Japan, 200 kV) were used to investigate the surface morphology, internal structure, and elemental compositions in the Center for University-Wide Research Facilities at the Jeonbuk National University. XPS (Theta Probe; Thermo Fisher Scientific, UK) was used to analyze the surface chemical compositions and the valence states of the elements. The SSA and pore-size distributions were evaluated, using the BET and BJH methods, at 77 K by performing a multipoint nitrogen adsorption–desorption experiment on an ASAP 2020 Plus system (Micromeritics Instrument Corp., USA) analyzer after degassing the samples at 100 °C for 15 h with the help of a dynamic vacuum.

Supporting Information

Supporting Information is available from the Wiley Online Library or from the author.

Acknowledgements

Conflict of Interest

The authors declare no conflict of interest.

Data Availability Statement

Research data are not shared.

Keywords

[1] J. A. Turner, *Science* **2004**, *305*, 972.
[2] T. Ling, D. Y. Yan, H. Wang, Y. Jiao, Z. Hu, Y. Zheng, L. Zheng, J. Mao, H. Liu, X. W. Du, M. Jaroniec, S. Z. Qiao, *Nat. Commun.* **2017**, *8*, 1.
[3] J. B. Gerken, J. G. McAlpin, J. Y. C. Chen, M. L. Rigsby, W. H. Casey, R. D. Britt, S. S. Stahl, *J. Am. Chem. Soc.* **2011**, *133*, 14431.
[4] Y. Jiao, Y. Zheng, M. Jaroniec, S. Z. Qiao, *Chem. Soc. Rev.* **2015**, *44*, 2060.
[5] F. Song, L. Bai, A. Moysiadou, S. Lee, C. Hu, L. Liardet, X. Hu, *J. Am. Chem. Soc.* **2018**, *140*, 7748.
[6] Y. Zheng, Y. Jiao, M. Jaroniec, S. Z. Qiao, *Angew. Chem., Int. Ed.* **2015**, *54*, 52.
[7] H. Jin, J. Wang, D. Su, Z. Wei, Z. Pang, Y. Wang, *J. Am. Chem. Soc.* **2015**, *137*, 2688..
[8] J. Wang, K. Li, H. X. Zhong, D. Xu, Z. L. Wang, Z. Jiang, Z. J. Wu, X. B. Zhang, *Angew. Chem., Int. Ed.* **2015**, *54*, 10530.
[9] T. I. Singh, G. Rajeshkhanna, S. B. Singh, T. Kshetri, N. H. Kim, J. H. Lee, *ChemSusChem* **2019**, *12*, 4810.
[10] T. I. Singh, G. Rajeshkhanna, T. Kshetri, N. H. Kim, J. H. Lee, *J. Mater. Chem. A* **2020**, *8*, 26158.
[11] T. Kshetri, T. I. Singh, Y. S. Lee, D. D. Khumujam, N. H. Kim, J. H. Lee, *Composites, Part B* **2021**, *211*, 108624.
[12] W. Yang, Z. Wang, W. Zhang, S. Guo, *Trends Chem.* **2019**, *1*, 259.
[13] R. Zhang, Y. C. Zhang, L. Pan, G. Q. Shen, N. Mahmood, Y. H. Ma, Y. Shi, W. Jia, L. Wang, X. Zhang, W. Xu, J. J. Zou, *ACS Catal.* **2018**, *8*, 3803.
[14] D. R. Paudel, U. N. Pan, T. I. Singh, C. C. Gudal, N. H. Kim, J. H. Lee, *Appl. Catal., B* **2021**, *286*, 119897.
[15] Z. Xiao, Y.-C. Huang, C.-L. Dong, C. Xie, Z. Liu, S. Du, W. Chen, D. Yan, L. Tao, Z. Shu, G. Zhang, H. Duan, Y. Wang, Y. Zou, R. Chen, S. Wang, *J. Am. Chem. Soc.* **2020**, *142*, 12087.
[16] J. Li, C. Shu, C. Liu, X. Chen, A. Hu, J. Long, *Small* **2020**, *16*, 1.
[17] Q. Wu, M. Xiao, W. Wang, C. Cui, *ACS Catal.* **2019**, *9*, 11734.
[18] N. Ortiz Peña, D. Ihiawakrim, M. Han, B. Lassalle-Kaiser, S. Carenco, C. Sanchez, C. Laberty-Robert, D. Portehault, O. Ersen, *ACS Nano* **2019**, *13*, 11372.
[19] M. S. Burke, M. G. Kast, L. Trotochaud, A. M. Smith, S. W. Boettcher, *J. Am. Chem. Soc.* **2015**, *137*, 3638.
[20] S. Liu, L. Li, N. A. Patterson, A. Manthiram, *J. Electrochem. Soc.* **2016**, *163*, A150.
[21] T. T. H. Hoang, Y. Cohen, A. A. Gewirth, *Anal. Chem.* **2014**, *86*, 11290.
[22] S. Jiao, X. Fu, L. Zhang, Y. J. Zeng, H. Huang, *Nano Today* **2020**, *31*, 100833.
[23] J. Yang, H. Liu, W. N. Martens, R. L. Frost, *J. Phys. Chem. C* **2010**, *114*, 111.
[24] Y. Li, W. Qiu, F. Qin, H. Fang, V. G. Hadjiev, D. Litvinov, J. Bao, *J. Phys. Chem. C* **2016**, *120*, 4511.
[25] A. Moysiadou, S. Lee, C. S. Hsu, H. M. Chen, X. Hu, *J. Am. Chem. Soc.* **2020**, *142*, 11901.
[26] Z. Kou, Z. Yu, X. Liu, X. Gao, L. Zheng, H. Zou, Y. Pang, Z. Wang, Z. Pan, J. He, S. J. Pennycook, J. Wang, *ACS Catal.* **2020**, *10*, 4411.
[27] K. S. Joya, X. Sala, *Phys. Chem. Chem. Phys.* **2015**, *17*, 21094.
[28] S. Bae, J. H. Cha, J. H. Lee, D. Y. Jung, *Dalton Trans.* **2015**, *44*, 16119.
[29] H. Zhang, J. Nai, L. Yu, X. W. (David) Lou, *Joule* **2017**, *1*, 77.
[30] Y. Zhang, L. Gao, E. J. M. Hensen, J. P. Hofmann, *ACS Energy Lett.* **2018**, *3*, 1360.
[31] S. Geiger, O. Kasian, M. Ledendecker, E. Pizzutilo, A. M. Mingers, W. T. Fu, O. Diaz-Morales, Z. Li, T. Oellers, L. Fruchter, A. Ludwig, K. J. J. Mayrhofer, M. T. M. Koper, S. Cherevko, *Nat. Catal.* **2018**, *1*, 508.
[32] F. D. Speck, K. E. Dettelbach, R. S. Sherbo, D. A. Salvatore, A. Huang, C. P. Berlinguette, *Chem* **2017**, *2*, 590.
[33] M. C. Biesinger, B. P. Payne, A. P. Grosvenor, L. W. M. Lau, A. R. Gerson, R. S. C. Smart, *Appl. Surf. Sci.* **2011**, *257*, 2717.
[34] G. Ou, F. Wu, K. Huang, N. Hussain, D. Zu, H. Wei, B. Ge, H. Yao, L. Liu, H. Li, Y. Shi, H. Wu, *ACS Appl. Mater. Interfaces* **2019**, *11*, 3978.
[35] J. Bao, X. Zhang, B. Fan, J. Zhang, M. Zhou, W. Yang, X. Hu, H. Wang, B. Pan, Y. Xie, *Angew. Chem., Int. Ed.* **2015**, *54*, 7399.
[36] A. A. Tahir, K. G. U. Wijayantha, S. Saremi-Yarahmadi, M. Mazhar, V. McKee, *Chem. Mater.* **2009**, *21*, 3763.

[37] H. Kong, J. Song, J. Jang, *Chem. Commun.* **2010**, *46*, 6735.

[38] M. Mullet, V. Khare, C. Ruby, *Surf. Interface Anal.* **2008**, *40*, 323.

[39] S.-F. Hung, Y.-Y. Hsu, C.-J. Chang, C.-S. Hsu, N.-T. Suen, T.-S. Chan, H. M. Chen, *Adv. Energy Mater.* **2018**, *8*, 1701686.

[40] S. H. Ye, Z. X. Shi, J. X. Feng, Y. X. Tong, G. R. Li, *Angew. Chem., Int. Ed.* **2018**, *57*, 2672.

[41] S. Kundu, B. Malik, D. K. Pattanayak, V. K. Pillai, *ACS Appl. Mater. Interfaces* **2017**, *9*, 38409.

[42] S. S. Shinde, C.-H. Lee, A. Sami, D.-H. Kim, S.-U. Lee, J.-H. Lee, *ACS Nano* **2017**, *11*, 347.

[43] N. Dwivedi, R. J. Yeo, N. Satyanarayana, S. Kundu, S. Tripathy, C. S. Bhatia, *Sci. Rep.* **2015**, *5*, 7772.

[44] H. Euchner, B. P. Vinayan, M. A. Reddy, M. Fichtner, A. Groß, *J. Mater. Chem. A* **2020**, *8*, 14205.

[45] Z. Chen, C. X. Kronawitter, B. E. Koel, *Phys. Chem. Chem. Phys.* **2015**, *17*, 29387.

[46] G. Rajeshkhanna, E. Umeshbabu, G. R. Rao, *J. Chem. Sci.* **2017**, *129*, 157.

[47] X.-C. Dong, H. Xu, X.-W. Wang, Y.-X. Huang, M. B. Chan-Park, H. Zhang, L.-H. Wang, W. Huang, P. Chen, *ACS Nano* **2012**, *6*, 3206.

[48] K. Fominykh, P. Chernev, I. Zaharieva, J. Sicklinger, G. Stefanic, M. Döblinger, A. Müller, A. Pokharel, S. Böcklein, C. Scheu, T. Bein, D. Fattakhova-Rohlfing, *ACS Nano* **2015**, *9*, 5180.

[49] L. Trotochaud, J. K. Ranney, K. N. Williams, S. W. Boettcher, *J. Am. Chem. Soc.* **2012**, *134*, 17253.

[50] S. Li, Y. Wang, S. Peng, L. Zhang, A. M. Al-Enizi, H. Zhang, X. Sun, G. Zheng, *Adv. Energy Mater.* **2016**, *6*, 1501661.

[51] Y. P. Zhu, Y. P. Liu, T. Z. Ren, Z. Y. Yuan, *Adv. Funct. Mater.* **2015**, *25*, 7337.

[52] Y. Liang, Y. Li, H. Wang, J. Zhou, J. Wang, T. Regier, H. Dai, *Nat. Mater.* **2011**, *10*, 780.

[53] Y. Guo, J. Tang, H. Qian, Z. Wang, Y. Yamauchi, *Chem. Mater.* **2017**, *29*, 5566.

[54] X. Han, C. Yu, S. Zhou, C. Zhao, H. Huang, X. Yang, Z. Liu, J. Zhao, J. Qiu, *Adv. Energy Mater.* **2017**, *7*, 1602148.

[55] J. Huang, J. Chen, T. Yao, J. He, S. Jiang, Z. Sun, Q. Liu, W. Cheng, F. Hu, Y. Jiang, Z. Pan, S. Wei, *Angew. Chem., Int. Ed.* **2015**, *54*, 8722.

[56] H. Jin, S. Mao, G. Zhan, F. Xu, X. Bao, Y. Wang, *J. Mater. Chem. A* **2017**, *5*, 1078.

[57] L. Feng, A. Li, Y. Li, J. Liu, L. Wang, L. Huang, Y. Wang, X. Ge, *ChemPlusChem* **2017**, *82*, 483.

[58] F. Song, X. Hu, *Nat. Commun.* **2014**, *5*, 1.

[59] J. Geng, L. Kuai, E. Kan, Q. Wang, B. Geng, *ChemSusChem* **2015**, *8*, 659.

[60] S. Zhao, M. Li, M. Han, D. Xu, J. Yang, Y. Lin, N. E. Shi, Y. Lu, R. Yang, B. Liu, Z. Dai, J. Bao, *Adv. Funct. Mater.* **2018**, *28*, 1706018.

[61] H. Jiang, Q. He, X. Li, X. Su, Y. Zhang, S. Chen, S. Zhang, G. Zhang, J. Jiang, Y. Luo, P. M. Ajayan, L. Song, *Adv. Mater.* **2019**, *31*, 1805127.

[62] G. Rajeshkhanna, T. I. Singh, N. H. Kim, J. H. Lee, *ACS Appl. Mater. Interfaces* **2018**, *10*, 42453.

[63] J. Song, C. Zhu, B. Z. Xu, S. Fu, M. H. Engelhard, R. Ye, D. Du, S. P. Beckman, Y. Lin, *Adv. Energy Mater.* **2017**, *7*, 1601555.

[64] F. Qin, Z. Zhao, M. K. Alam, Y. Ni, F. Robles-Hernandez, L. Yu, S. Chen, Z. Ren, Z. Wang, J. Bao, *ACS Energy Lett.* **2018**, *3*, 546.

[65] N. Dubouis, A. Grimaud, *Chem. Sci.* **2019**, *10*, 9165.

[66] S. C. Petitto, E. M. Marsh, G. A. Carson, M. A. Langell, *J. Mol. Catal. A: Chem.* **2008**, *281*, 49.

[67] X. Wang, Z. Li, D.-Y. Wu, G.-R. Shen, C. Zou, Y. Feng, H. Liu, C.-K. Dong, X.-W. Du, *Small* **2019**, *15*, 1804832.

[68] Q. Xu, H. Jiang, X. Duan, Z. Jiang, Y. Hu, S. W. Boettcher, W. Zhang, S. Guo, C. Li, *Nano Lett.* **2021**, *21*, 492.

[69] C. Wei, S. Sun, D. Mandler, X. Wang, S. Z. Qiao, Z. J. Xu, *Chem. Soc. Rev.* **2019**, *48*, 2518.